IEEE Access
Multidisciplinary | Rapid Review | Open Access Journal

Received 31 December 2022, accepted 28 January 2023, date of publication 6 March 2023, date of current version 24 April 2023.

Digital Object Identifier 10.1109/ACCESS.2023.3253482

RESEARCH ARTICLE

A BIM-Based Algorithm for Quantitative Monitoring of Temperature Distribution During Breast Hyperthermia Treatments

HULUSI ONAL, TUBA YILMAZ, (Member, IEEE), AND MEHMET NURI AKINCI
Department of Electronics and Communication Engineering, Istanbul Technical University, 34485 Istanbul, Türkiye

Corresponding author: Mehmet Nuri Akinci (akincime@itu.edu.tr)

This work was supported by the Scientific and Technological Research Council of Turkey under Grant 118S074.

ABSTRACT Microwave hyperthermia (MH) treatment for breast cancer is a research interest due to its capability to initiate cell necrosis in malignant tumor or to enhance the effect of other treatment modalities such as chemotherapy. The goal of MH treatment is to increase temperature of malignant tumor up to 45°C based on the treatment plan; however, microwave energy focusing is a challenging problem and may cause unwanted hotspots on healthy tissues; therefore, there is a need to monitor the temperature. In this paper, an iterative differential microwave imaging algorithm for temperature monitoring is presented. The algorithm is based on Born iterative method (BIM) and Tikhonov regularization. Feasibility of the algorithm is shown by a large computational study using realistic digital breast phantoms via TM_z polarized 2-D scattered fields. Also, some results are given for calibrated scattering parameters, which are obtained from both a 3-D electromagnetic simulation program and a simple measurement setup. An approach for selection of matching medium in hyperthermia monitoring applications is also presented. The reconstructions are performed with scattered field data collected at 11 discrete frequency points uniformly taken from the 0.5-1.5 GHz range. For a specific heating scenario in 2-D problem, reconstruction error is lower than 0.3% with ±10% noise on reference dielectric property distribution and 40 dB signal to noise ratio (SNR). The results show that the proposed approach provides up to 3°C and 0.1°C resolution in temperature estimation with ±10% noise on reference dielectric property distribution for 30 dB and 60 dB SNR values, respectively.

INDEX TERMS Breast imaging, hyperthermia, electromagnetic inverse scattering, microwave imaging, temperature monitoring.

I. INTRODUCTION

Microwave hyperthermic treatments aim to increase the temperature of the malignant tumor for cell destruction and can be categorized under two main approaches microwave hyperthermia (MH) and microwave ablation (MWA) [1], [2], [3]. Microwave hyperthermia (MH) is a non-invasive technique that can either be used as a sole treatment method to raise the tumor temperatures up to 45°C or as a complimentary treatment method to other therapies such as chemotherapy for heating the target tissue to relatively lower temperatures (below 42°C) [4], [5], [6], [7].

The associate editor coordinating the review of this manuscript and approving it for publication was Chan Hwang See.

Non-invasive focusing in MH is achieved trough the optimization of the antenna excitations surrounding the target tissues [8]. Relatively higher dielectric properties of tumor tissues, particularly conductivity, in comparison to normal tissues also contribute to the effective heating [6], [9]. Despite the inherent conductivity discrepancy and source optimization, the spreading propagation behavior of EM waves and tissue heterogeneity in the target region may prevent the effective heating of the tumor tissue. Especially, undesirable hotspots, commonly accepted as higher than 40°C [10], [11], may occur on healthy tissues, which leads to unwanted destruction of healthy cells. Therefore, it is vital to monitor the heating at the target region to ensure safe and effective treatment [10]. Towards this goal, many

different thermal monitoring techniques have been proposed in the literature that can be categorized as passive and active techniques.

Among passive microwave techniques radiometry was utilized to monitor temperature variations; however, such techniques provide only surface temperature values and suffer from poor sensitivity. Therefore, passive techniques are challenging to be utilized for real-time imaging [12]. Active techniques are ultrasound (US) [13], [14], [15], magnetic resonance imaging (MRI) [16], [17], [18], and microwave tomography (MWT) [19], [20], [21] have been proposed to be used for temperature monitoring applications. Limitations of these methods are similar to their use in diagnostics based imaging applications. For example, MRI based methods generally provide good accuracy but MRI is known to be very costly and bulky [22], [23]. While the US based methods are low-cost and can be implemented for real time imaging, they are known to suffer from major drawbacks related with motion artifacts and water vaporization [24], [25]. Among active techniques, MWT is emerging as a promising approach for thermal monitoring.

It is known that MWT methods tend to be computationally expensive; however, in comparison to other active methods MWT is relatively low-cost and can be implemented as a portable device [22], [26]. Similar to the conventional use of MWT for biomedical diagnostics, MWT exploits the inherent dielectric property discrepancy occurring in tissues due to temperature change during thermal treatment. One such application where MWT is applied in a similar manner is contrast-enhanced breast tumor imaging [27], [28], in which it is assumed that the tumor dielectric properties are modified via an external effect named contrast agent. Then, the dielectric property discrepancy before and after the injection of the contrast agent is reconstructed through differential imaging. Although the contrast enhancement successfully applied to reconstruction of tumor location and the shape, the methods are still unable to provide quantitative imaging with accurate dielectric profile of the target medium. The MWT is also applied to monitor the microwave ablation (MWA) applications. Different from MH, in MWA, the tissue is heated to larger temperatures where the dielectric property variation is also large. Another difference from MH is MWA performs invasive and local heating. Therefore, focused MWT is often used for thermal monitoring during MWA. The proposed MWT studies either fail to reconstruct the accurate dielectric values of the target tissues [22] or do not address small variations in temperature [20]. In another study [2], experimental results with a simple breast phantom are presented where the feasibility of thermal monitoring approaches is investigated. The study generally focuses on qualitative estimation of temperature, even though a few results are also given to correlate temperature and dielectric properties. Nevertheless, the study does not focus on inhomogeneous targets; therefore, the issues originating from highly inhomogeneous structure of a breast are not addressed. In [21], an updated version of [2], is proposed where dielectric properties of the target medium were quantitatively reconstructed using distorted Born iterative method (DBIM). However, this approach is shown to work for localized large temperature discrepancies similar to thermal monitoring of MWA. Instead, we also focus on temperature variations, which are very small and distributed over the imaging domain. Additionally, the method in [21] requires solution of direct scattering problem for each iteration step in the reconstruction process. To overcome this limitation, the study utilized cutting-edge GPUs for parallel computation but the approach increases the cost of the monitoring system. Contrary to this, our BIM based algorithm does not need to solve direct scattering problem during the iterative process, which highly decreases the computational cost.

Considering the previously reported studies and the requirements of the thermal monitoring for MH, it can be concluded that the success of the thermal monitoring can be determined by evaluating three main indicators. First, the proposed method must provide quantitative information with sufficient accuracy to ensure the effective treatment via establishing a feedback loop between the MWT and MH systems. Next, algorithm must enable real-time thermal monitoring since a lagged detection leads to safety concerns. Finally, modelling of the temperature variations must be compatible with the target temperatures in MH applications. Since the temperature change is rather smaller in MH, the corresponding dielectric property change is also expected to be small. Therefore, there is a need to develop algorithms and measurement setup sensitive to the small dielectric property changes. To enable sensitive MWT during imaging of inhomogeneous medium such as biological tissue, usually a matching medium is utilized. The matching medium is known to improve the imaging sensitivity. Previously reported studies used different mediums including non-conductive ones; however, the reported ones are not suitable for MH monitoring due to high sensitivity requirements [29], [30], [31]. Therefore, to meet the thermal monitoring requirements during MH, there is a need to investigate the matching medium properties in order to increase the sensitivity of the MWT system.

This paper presents an approach based on Born iterative method (BIM) for monitoring temperature variations and its feasibility in breast cancer hypertermia treatment. Two dimensional (2-D) analysis with TM_z polarization is applied to realistic numerical breast phantoms utilizing temperature-dependent dielectric properties. Feasibility of the method is also shown by calibrated scattered field data from a 3-D simulation software and a simple measurement setup. The contributions of this paper are as follows:

- A model representing the relationship between the temperature and dielectric properties of biological tissue is proposed for hyperthermia applications. This enables us to construct a certain relation between temperature and dielectric properties of the tissues over the highly inhomogeneous imaging domain. Therefore, the proposed method can also detect simultaneous

temperature changes in different regions of the imaging domain.
- The equations are modified to produce maps of temperature distributions, and we have experienced that this approach improves the results in comparison to the external mapping of dielectric properties to temperature. This is because the temperature dependencies of dielectric constant and effective conductivity are directly inserted into the inversion equations.
- The issues originating from tiny variations in dielectric properties due to temperature are addressed. The analysis reveals the importance of matching medium for such a problem. Based on this, an approach for matching medium selection specifically for hyperthermia monitoring applications is also presented.

The paper is organized as follows. In Section II-A, frequency and temperature dependencies of some tissues presented in literature are given and a modelling approach for temperature effect on breast tissues is proposed. The mathematical formulations for the direct and inverse scattering methods are given in Section II-B. A method for the selection of a matching medium is given in Section II-C. The results obtained from 2-D data are given in Section III-A, and the results for the data, which are calibrated from the 3-D simulation software and the measurement setup, are given in Section III-B and Section III-C, respectively. The paper is ended with conclusion in Section IV. Note that $e^{-j\omega t}$ time dependency is used throughout the paper.

II. METHOD

A. MODELLING OF THE IMAGING DOMAIN AND THERMAL VARIATIONS

1) BREAST MODEL

In this work, realistic breast phantoms presented in [32] and [33] by University of Wisconsin Cross-Disciplinary Electromagnetics Laboratory are used. The main disribution used in this study is the 96*th* vertical cross section from a heterogeneously dense phantom with Breast ID: 062204. Another distribution is 159*th* vertical cross section from a scattered fibroglandular phantom with Breast ID: 012204. Dielectric constant and effective conductivity distributions for these cross sections are given in Fig. 1.

As it is seen from the Fig. 1, the selected cross sections serve different properties in terms of density of the glandular tissues. This is important to present a more comprehensive computational study because it can be considered that each distribution belongs to a different patient having different breast properties. All models have 1.5 mm resolution and same resolution is used during direct scattering simulation that are performed for data acquisition. However, during the inversion procedure, 2 mm resolution is used in order to avoid inverse crime case.

2) BREAST TUMOR

Tumor is modelled as a homogeneous circle with a given radius ranging from 0.5 cm to 1 cm for all simulations. These

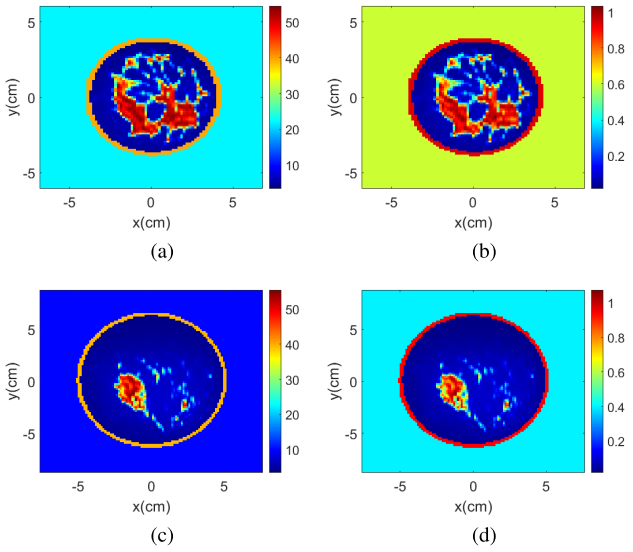

FIGURE 1. Dielectric constant (left column) and effective conductivity (right column) distributions of 2-D cross sections from the selected breast phantoms at 1 GHz: (a)-(b) ID: 062204, (c)-(d) ID: 012204.

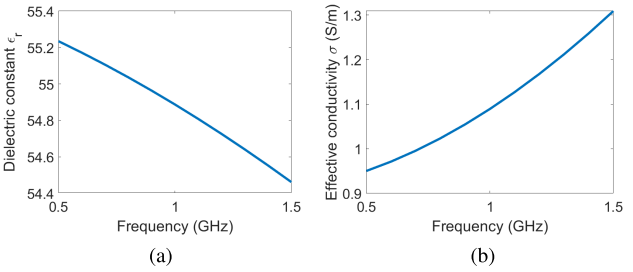

FIGURE 2. Dielectric property variation of breast tumor with respect to frequency between 0.5-1.5 GHz. (a) Dielectric constant, (b) effective conductivity.

values can be seen as suitable dimensions to represent breast tumors [34].

The dielectric constant and effective conductivity variations with respect to frequency for breast tumor are tabulated in the literature [33], [35]. Both studies provide Cole-Cole parameters which models the frequency dispersive dielectric properties when inserted to the Cole-Cole equation [36]. For this work, model given in [35] is used, and we note that both studies provide similar results. The data presented in [35] are given in Fig. 2.

3) TEMPERATURE DEPENDENCY OF TISSUES

It is known that dielectric properties of tissues depend on temperature. However, to the best of the authors' knowledge, there is no study providing a model for temperature-dependent breast tissue dielectric properties due to the challenges associated with performing experiments on real breast tissues. Nonetheless, there are studies reporting the temperature-dependent dielectric properties of animal tissues such as bovine and porcine [37], [38]. Since tissues can be classified based on the water content, the animal tissue

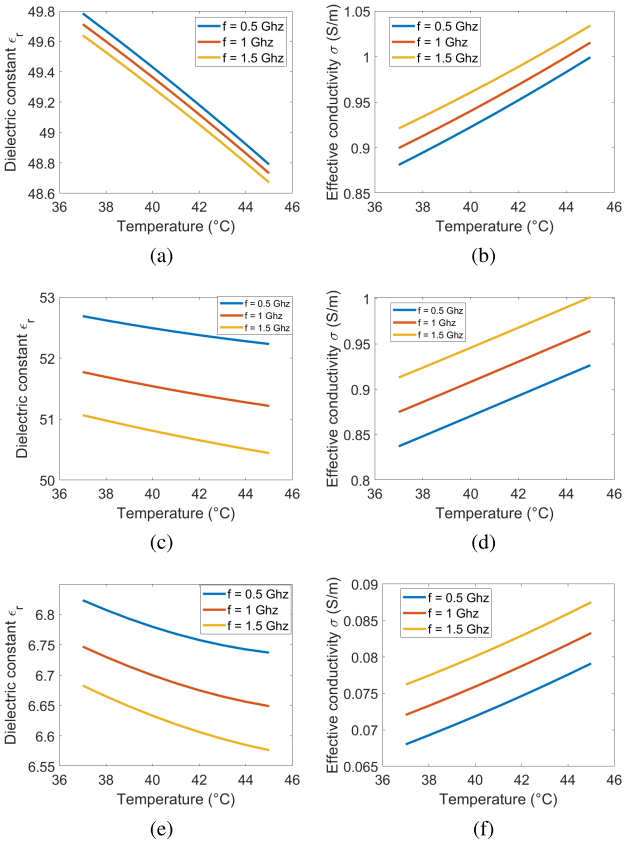

FIGURE 3. Dielectric property variation of some animal tissues with respect to temperature at specific frequencies. (a)-(b) Liver presented in [38]. (c)-(d) Liver presented in [37]. (e)-(f) Fat represented in [37].

models are used in this work [37]. In [38], bovine and porcine liver tissues are investigated and Cole-Cole parameters are given as polynomials of temperature. A similar study is presented in [37], Cole-Cole parameters as polynomials with temperature as a variable also given for liver, muscle, fat, and blood tissues of porcine. Among these models, we focused on the data given for liver and fat tissues. Both the liver tissue and tumor tissues are categorized under high water content tissues. Similarly, fat and breast fat are categorized under low water content tissues. Thus, the dielectric properties of these tissues are similar. Therefore, temperature-dependent data on porcine fat tissue given in [37] is considered for breast fat. Temperature-dependent dielectric properties of liver and fat given in [38] and [37] are shown in Fig. 3.

On the other hand, it must be noted that the realistic breast models used in this work have a very large variety of the dielectric constant and effective conductivity. Therefore, it is not possible to match these values with data given the references directly. For the sake of simplicity, a common approach for temperature dependency of all cells in breast model has been accepted for this study. Firstly, if variations in Fig. 3 are considered, it can be said that dielectric properties are almost linearly correlated with the temperature for all type of tissues in relevant frequencies. If these relationships are accepted as linear, dielectric constant and effective conductivity changes per temperature can be computed. If Fig. 3(a)-(b) is considered, total percentage changes from 37°C to 45°C at 0.5, 1, and 1.5 GHz can be computed as −1.997%, −1.975%, −1.951%. Also for conductivity variation, percentage values can be computed as +13.408%, +12.860%, +12.256%. If Fig. 3(c)-(d) is considered, the variations can be computed as −0.867%, −1.073%, −1.219% for dielectric constant, and +10.669%, +10.199%, +9.689% for effective conductivity. Lastly, if Fig. 3(e)-(f) is considered, the variations can be computed as −1.264%, −1.453%, −1.590% for dielectric constant, and +16.312%, +15.391%, +14.843% for effective conductivity. Based on these observations, it is reasonable to choose approximate coefficients associating dielectric properties with temperature. These coefficients are selected as -2% for dielectric constant and +10% for effective conductivity. This means we assume that -0.25% change on dielectric constant and +1.25% change on effective conductivity per 1°C increase on the temperature. Thus, the temperature-dependent dielectric constant and conductivity of the breast tissues are given as follows.

$$\epsilon_r(r,T) = \epsilon_r(r,37^\circ) \times \left(1 - \frac{T-37^\circ}{8^\circ} \times \frac{2}{100}\right) \quad (1)$$

$$\sigma(r,T) = \sigma(r,37^\circ) \times \left(1 + \frac{T-37^\circ}{8^\circ} \times \frac{10}{100}\right) \quad (2)$$

4) GENERATION OF A HEATING SCENARIO

The approach relating temperature and dielectric properties has been defined in previous section. Based on this way, heating scenarios are generated. As stated before, geometry of the tumor is circle, and it is replaced on a specific location for a specific model. Geometry of heated regions on the breast are also selected as circles. To prevent abrupt heat jumps on boundary of heating regions, heating effects on the selected regions are modelled with 3 cylindrical layers such that when temperature increases on inner layer the amount of T °C, the temperature rise on the second (intermediate) layer is 0.75T °C and third (outer) layer is 0.5T °C. It is important to note that the heating studies in the literature demonstrate the plausibility of our temperature change model [8], [39], [40].

An example heating scenario where temperature raises from 37°C up to 45°C on 062204 model is given in Fig. 4. First, a hotspot location is selected on a glandular dense region where dielectric properties are higher than fatty tissue regions. Another high temperature location is assumed to be the tumor. Then, temperature map for the heated case is obtained as in Fig. 4(b). In this figure, 45°C indicates the top temperature value on the heated regions and there is a gradual decrease in temperature due to the layered modelling. For this specific figure, the temperature level for the inner layer is 45°C and corresponding dielectric constant and effective conductivity changes are -2% and +10%, respectively. For the intermediate layer dielectric

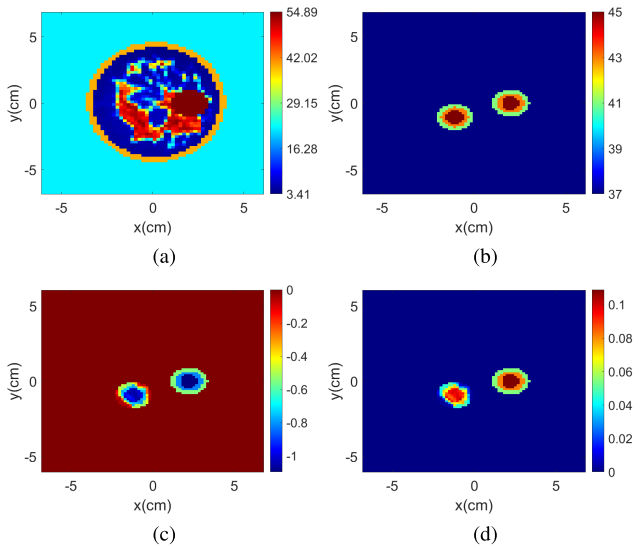

FIGURE 4. (a) Dielectric constant distribution of 062204 model with tumor inclusion. (b) Temperature distribution in an example heated scenario (°C). Corresponding change in value of (c) dielectric constant and (d) effective conductivity due to the variation of temperature from 37°C up to 45°C.

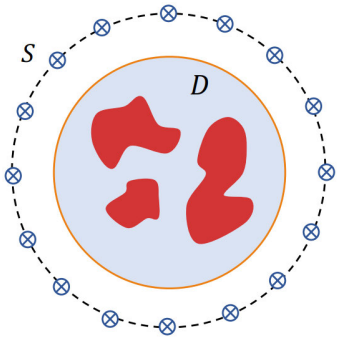

FIGURE 5. General configuration of 2-D EM scattering problem. The cross shaped circles show transmitter/receiver locations.

constant and effective conductivity changes are $(-2\%) \times (0.75) = -1.5\%$ and $(+10\%) \times (0.75) = +7.5\%$, respectively. Finally, for the third layer dielectric constant and effective conductivity changes are $(-2\%) \times (0.5) = -1\%$ and $(+10\%) \times (0.5) = +5\%$, respectively. The map of variations in the values of dielectric constant and effective conductivity are given in Fig. 4(c) and Fig. 4(d), respectively. Same rates are valid for radius of layers. That is, for a 1 cm tumor, inner layer comprises circular region with a radius of $(1) \times (0.5) = 0.5$ cm, intermediate layer comprises intermediate region between 0.5 cm and $(1) \times (0.75) = 0.75$ cm, and outer layer comprises the region between 0.75 cm and 1 cm.

B. MATHEMATICAL FORMULATION

1) DIRECT SCATTERING SIMULATIONS

In order to simulate the measurement data, a commonly used numerical technique named as Method of Moments (MoM) is used. MoM is implemented using a well-known method based on the pulse basis functions described in [41]. The MoM reduces the integral equation to a matrix equation. Then, total field on the each cell in the computation domain can be determined by solving this system of equations. General configuration for 2-D electromagnetic scattering problem can be seen in Fig. 5. In this figure, S denotes discrete points on a circle where transmitter and receiver antennas have been settled, and cross shaped circles indicate the antennas. D is computation domain containing breast interior. Then, following equation indicating that total field is equal to sum of incident and scattered fields is satisfied every point in computation domain D [42].

$$E(r, r'; \omega) = E_i(r, r'; \omega) + k_0^2(\omega) \int_D G(r'', r; \omega)\xi(r; \omega)E(r, r'; \omega)dr, \quad r'' \in D \tag{3}$$

Discretization of (3) leads to the $N \times N$ linear system of equations where N denotes number of cells in computation domain, and solution of this equation gives the total field E on every point in the computation domain D. Once the total field is computed, scattered field can be easily determined by the following equation.

$$E_s(r'', r'; \omega) = k_0^2(\omega) \int_D G(r'', r; \omega)\xi(r; \omega)E(r, r'; \omega)dr, \quad r'' \in S \tag{4}$$

In these equations, $r \in \mathbb{R}^N$ denotes the source points indicating the locations of induced current sources on domain D. The vector $r' \in \mathbb{R}^T$ denotes locations of transmitters, in which T denotes number of transmitters. And, r'' can be called as observation points, which denotes the points in domain D in (3), i.e., $r'' \in \mathbb{R}^N$, and receiver locations in (4), i.e., $r'' \in \mathbb{R}^R$, where R denotes number of receivers.

These two main equations (3) and (4) given above can be written in a compact form as shown below.

$$E = E_i + k_0^2 G_D (E\xi) \tag{5}$$

$$E_s = k_0^2 G_S (E\xi) \tag{6}$$

Here, E is a $N \times T$ matrix carrying the total field values on every cell caused by each transmitter. E_i is also a $N \times T$ matrix representing incident field values on every cell. E_s is the scattered field matrix with $R \times T$ dimension. G is Green's function given by $G(r'', r; \omega) = (i/4)H_0^{(1)}(k_b|r'' - r|)$ where $k_b(\omega) = \sqrt{\omega^2 \epsilon_{r_b} \epsilon_0 \mu_0 + i\omega\mu_0\sigma_b}$ is wavenumber in matching medium. In (5), the Green's function G_D relates the source cells and observation cells in computation domain; thus, it is a $N \times N$ matrix. In (6), G_S relates the receivers in domain S and the source cells in domain D, and it is a $R \times N$ matrix. k_0 is the wavenumber of free-space given by $k_0(\omega) = \omega/c$ where c is speed of light. Note that all of these quantities are frequency dependent; therefore, they have also one more index F which shows the frequency dependency, but it is not written here for simplicity. ξ is a $N \times 1$ contrast vector defined as $\xi(r) = \epsilon_r^c(r; \omega) - \epsilon_{r_b}^c(\omega)$ where ϵ_r^c and $\epsilon_{r_b}^c$ denote complex

dielectric constant of cells in domain D and in matching medium, respectively. Complex dielectric constant is given as $\epsilon_r^c = \epsilon_r + i\sigma/(\omega\epsilon_0)$. Here, ϵ_r and σ denote dielectric constant and effective conductivity, respectively. Throughout this paper, dielectric properties of a material or tissue refer these two quantities.

In this study, there are 16 antennas [30] placed on a circle with a radius of 7.5 cm, and they are modelled as line sources. While one antenna transmits, others are considered as receivers. This means $R = T = 16$; therefore, obtained scattered field data are 16×16 matrix. During this work, multi-frequency data are used, and number of frequency points is selected as $F = 11$ between 0.5 and 1.5 GHz with 100 MHz resolution. We have observed that higher frequencies decrease the accuracy of the results due to lower penetration of EM waves into breast as also reported in [30], and frequency resolution does not have remarkable effect on the accuracy.

2) INVERSION VIA THE PROPOSED METHOD

After obtaining the scattered field through the solution of direct scattering problem, these data are used to reconstruct the temperature maps on the investigation domain via solving the inverse scattering problem. This problem is ill-posed [43], similar to other medical imaging problems, and the approach used to solve the problem at hand is explained in the remainder of this section.

Before the inversion procedure, it is assumed that a dielectric property distribution was obtained through MRI. This is generally common assumption in studies about quantitative estimation of temperature on inhomogeneous scatterers [21]. Besides, it is not a strict assumption if it is remembered that the breast models used in this study are also derived from MRI. The reference distribution is patient specific, and allows us to compute a reference total field distribution using the direct solver. Based on these assumptions, kernel of the linearized version of the scattering equation is constructed with Green's function of the background and total field of the reference distribution of patient's breast. This linearization can be considered as Born approximation [44] which is carried out with a reference total field distribution instead of incident field. To write the system in standard form, the matrices are concatenated as [45],

$$A_{1+(m-1)R:mR,:,f} = k_0^2 G_{s_{:,:,f}} \odot {E^{ref}_{:,m,f}}^T \tag{7}$$

$$b_{1+(m-1)R:mR,f} = \Delta E_{s_{:,m,f}} \tag{8}$$

where $m \in \{1, 2, 3, \ldots, 16\}$ indicates transmitters and receivers. $\Delta E_s = E_s^{hot} - E_s^{ref}$ represents the difference between measured scattered field from heated breast and the breast at the normal temperature, respectively. And, E^{ref} denotes the total field obtained via the direct scattering solution of reference distribution $\boldsymbol{\xi}^{ref}$. Subscript f indicates frequency dependent nature of these elements. In addition, $\odot$ symbol denotes element-wise multiplication where each row of G_s matrix are multiplied by mth column of E^{ref} matrix. After these operations, A becomes $RT \times N \times F$ matrix, and b becomes $RT \times F$ matrix. Multi-frequency reconstruction is performed in this work because it enhances the accuracy of the solution [46]. Also, the dielectric properties of biological tissues are inherently frequency dispersive; thus, it is also important to arrange the equation such that dispersive effects are also considered. This approach mitigates the complications arising from the ill-posed nature of the problem [30], [47]. Therefore, it is expected to increase accuracy of the solution. New form of the equation is given below.

$$\begin{bmatrix} Re\{A_1\} & -\frac{Im\{A_1\}}{\omega_1\epsilon_0} \\ Im\{A_1\} & \frac{Re\{A_1\}}{\omega_1\epsilon_0} \\ Re\{A_2\} & -\frac{Im\{A_2\}}{\omega_2\epsilon_0} \\ Im\{A_2\} & \frac{Re\{A_2\}}{\omega_2\epsilon_0} \\ \vdots & \vdots \\ Re\{A_F\} & -\frac{Im\{A_F\}}{\omega_F\epsilon_0} \\ Im\{A_F\} & \frac{Re\{A_F\}}{\omega_F\epsilon_0} \end{bmatrix} \begin{bmatrix} \delta\boldsymbol{\epsilon}_r \\ \delta\boldsymbol{\sigma} \end{bmatrix} \approx \begin{bmatrix} Re\{\delta\boldsymbol{b}_1\} \\ Im\{\delta\boldsymbol{b}_1\} \\ Re\{\delta\boldsymbol{b}_2\} \\ Im\{\delta\boldsymbol{b}_2\} \\ \vdots \\ Re\{\delta\boldsymbol{b}_F\} \\ Im\{\delta\boldsymbol{b}_F\} \end{bmatrix} \tag{9}$$

And, in compact form

$$[B]_{2RTF\times 2N}\,[\delta\boldsymbol{\rho}]_{2N\times 1} \approx [\delta\boldsymbol{c}]_{2RTF\times 1}\,. \tag{10}$$

In equation (10), $\delta\boldsymbol{\rho} = [\delta\boldsymbol{\epsilon}_r, \delta\boldsymbol{\sigma}]$ is a $2N \times 1$ vector. Since the relations between temperature and dielectric properties are known, this equation can be rearranged to give the temperature difference. Based on (1) and (2), tissue dielectric property and temperature relations can be expressed as follows:

$$\delta T(r) = \delta T_{\epsilon_r}(r) = -\left(\frac{\delta\epsilon_r(r)}{\epsilon_r(r,\omega)}100\right)\frac{8}{2} \tag{11}$$

$$\delta T(r) = \delta T_{\sigma}(r) = \left(\frac{\delta\sigma(r)}{\sigma(r,\omega)}100\right)\frac{8}{10} \tag{12}$$

Then, vectors combining dielectric properties and temperature variation can be written as follows:

$$\kappa_f^{\epsilon_r}(r) = \frac{\delta\epsilon_r(r)}{\delta T_{\epsilon_r}(r)} = -0.25\times 10^{-2}\epsilon_r(r,\omega) \tag{13}$$

$$\kappa_f^{\sigma}(r) = \frac{\delta\sigma(r)}{\delta T_{\sigma}(r)} = 1.25\times 10^{-2}\sigma(r,\omega) \tag{14}$$

Notice that, $\delta\boldsymbol{T}_{\epsilon_r} = \delta\boldsymbol{T}_{\sigma} = \delta\boldsymbol{T}$. In these equations, all the quantities are vectors with length of N. And, $\boldsymbol{\kappa}_f^{\epsilon_r}$ and $\boldsymbol{\kappa}_f^{\sigma}$ are coefficient vectors defining the relation between temperature and dielectric property changes for each cell in computation domain. Once these expressions are inserted

to (9), the equation takes the form of (15).

$$\begin{bmatrix} \kappa_1^{\epsilon_r} Re\{A_1\} - \frac{\kappa_1^{\sigma}}{\omega_1 \epsilon_0} Im\{A_1\} \\ \kappa_1^{\epsilon_r} Im\{A_1\} + \frac{\kappa_1^{\sigma}}{\omega_1 \epsilon_0} Re\{A_1\} \\ \kappa_2^{\epsilon_r} Re\{A_2\} - \frac{\kappa_2^{\sigma}}{\omega_2 \epsilon_0} Im\{A_2\} \\ \kappa_2^{\epsilon_r} Im\{A_2\} + \frac{\kappa_2^{\sigma}}{\omega_2 \epsilon_0} Re\{A_2\} \\ \vdots \\ \kappa_F^{\epsilon_r} Re\{A_F\} - \frac{\kappa_F^{\sigma}}{\omega_F \epsilon_0} Im\{A_F\} \\ \kappa_F^{\epsilon_r} Im\{A_F\} + \frac{\kappa_F^{\sigma}}{\omega_F \epsilon_0} Re\{A_F\} \end{bmatrix} \left[\delta \boldsymbol{T}\right] \approx \begin{bmatrix} Re\{\delta \boldsymbol{b}_1\} \\ Im\{\delta \boldsymbol{b}_1\} \\ Re\{\delta \boldsymbol{b}_2\} \\ Im\{\delta \boldsymbol{b}_2\} \\ \vdots \\ Re\{\delta \boldsymbol{b}_F\} \\ Im\{\delta \boldsymbol{b}_F\} \end{bmatrix} \tag{15}$$

Equation (15) can be expressed in compact form as follows:

$$\left[C\right]_{2RTF \times N} \left[\delta \boldsymbol{T}\right]_{N \times 1} \approx \left[\delta \boldsymbol{c}\right]_{2RTF \times 1} \tag{16}$$

The problem given by (16) is ill-posed; therefore, it is required to apply regularization to obtain expected results. We use Tikhonov regularization which is given as follows [48], [49]:

$$\delta \boldsymbol{T} = \sum_{i=1}^{N} \frac{\sigma_i}{\sigma_i^2 + \alpha} (\boldsymbol{u}_i^T \cdot \delta \boldsymbol{c}) \boldsymbol{v}_i \tag{17}$$

where σ_i, $\boldsymbol{u}_i$, and $\boldsymbol{v}_i$ denote singular values, left singular vectors, and right singular vectors of matrix C, respectively. Also, α indicates the regularization parameter. The solution may highly depend on this parameter [50]; consequently, selection of this parameter is a crucial task. In this work, we have used the L-curve method [51] to determine appropriate value for regularization parameter. The implementation given in [52] generally provides stable results, and decreases required number of iteration significantly in an iterative process because it searches optimum value for the regularization parameter. Another method for selection of regularization parameter would be the Morozov's discrepancy principle. However, this method requires a priori knowledge about the noise level, and the solution highly depends on the estimation of the noise level. This is highly undesirable for applications where the signal and noise level are very close to each other, as in this study. Therefore, the L-curve method has been preferred.

Equation (17) gives the temperature difference. Nevertheless, it is generally not possible to obtain an accurate quantitative result with single solution. Therefore, BIM [53] which is an iterative algorithm is applied here. In every iteration step, total temperature difference vector is updated by solving (16),

$$\Delta \boldsymbol{T}^{(n)} = \Delta \boldsymbol{T}^{(n-1)} + \delta \boldsymbol{T}^{(n)} \tag{18}$$

where $n = 1, 2, 3, \ldots, N_{max}$. Thus, n indicates iteration step, and N_{max} is the maximum number of iteration. $\Delta \boldsymbol{T}^{(0)}$ denotes the total temperature variation vector at the start of the iteration; therefore, it is a zero vector. Also, $\delta \boldsymbol{T}$ indicates constrained temperature difference. The constraint can be given as,

$$\delta \boldsymbol{T}^{(n)} \succeq 0 \tag{19}$$

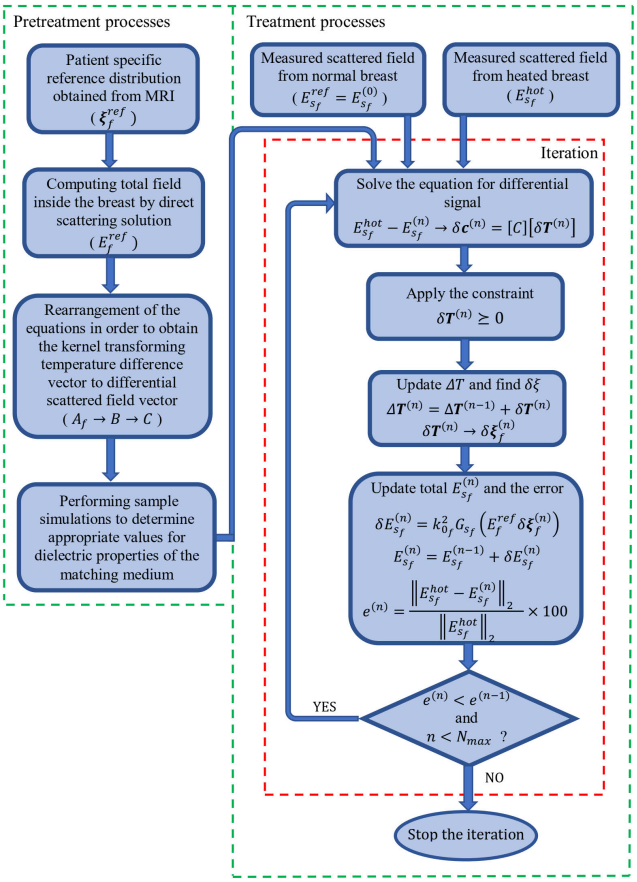

FIGURE 6. Flowchart of the approach presented in this paper.

where $\succeq$ symbol denotes element-wise inequality. Accordingly, any cell with a decreasing temperature will be avoided during the heating process. Next, by using equations (13) and (14), corresponding changes in dielectric properties can be computed. Then, the change in contrast vector which is also equal to change in complex dielectric constant can be determined by the following expression.

$$\delta \boldsymbol{\xi}_f{}^{(n)} = \delta \boldsymbol{\epsilon}_{rf}{}^{(n)} + i \frac{\delta \boldsymbol{\sigma}_f{}^{(n)}}{\omega_f \epsilon_0} \tag{20}$$

After that, scattered field is updated for every frequency as a direct multiplication of $\delta \boldsymbol{\xi}_f$ as in (21) and (22).

$$\delta E_{s_f}^{(n)} = k_{0_f}^2 G_{s_f} \left(E_f^{ref} \delta \boldsymbol{\xi}_f{}^{(n)} \right) \tag{21}$$

$$E_{s_f}^{(n)} = E_{s_f}^{(n-1)} + \delta E_{s_f}^{(n)} \tag{22}$$

Note that $E_{s_f}^{(0)}$ is the scattered field matrix at the start of the process; therefore, it indicates measured scattered field from patient breast at normal temperature level or namely cold case. After the update of the scattered field, the cost function is computed with the following equation,

$$e^{(n)}(\%) = \frac{\| E_{s_f}^{hot} - E_{s_f}^{(n)} \|_2}{\| E_{s_f}^{hot} \|_2} \times 100 \tag{23}$$

where $\|.\|_2$ symbol denotes Euclidean norm. The iteration process is terminated when the residual error starts to increase or maximum number of iterations is reached; otherwise, the iterative process continues with updated differential scattered field given with $E_{sf}^{hot} - E_{sf}^{(n)}$. Once the iterative process is finalized, the temperature distribution for a time t is determined by,

$$T_t(r) = T_{ref}(r) + \Delta T(r) \tag{24}$$

where T_{ref} denotes the temperature distribution at reference or normal temperature and is assigned the temperature value of 37°C.

The system repeats the process for scattered field measurement at every time t to determine the temperature distribution. The simplicity and speed of the approach stem from its ability to omit the direct scattering computations since each element, except from the scattered field measured at time t, are taken from reference distribution in which elements are computed or measured before the treatment process. The flowchart summarizing the steps stated in this section is given in Fig. 6.

C. MATCHING MEDIUM SELECTION

It is vital to determine proper matching medium in order to increase penetration of the EM waves into the breast interior. In problems similar to hyperthermia monitoring, selection of matching medium is of high importance due to the limited change in dielectric properties with temperature. During this work, we observed that if difference in scattered fields from normal and heated cases is under a certain level, obtained solution using this difference vector directly diverges or does not give any meaningful result. This is potentially due to the below noise level signal of the differential scattered field that corrupts the solution [50], [54]. The low level differential signal is originating likely from poor penetration of the EM waves into the breast. Therefore, we proposed an approach based on sweep analysis focusing on differential signal level using the function given in (25).

$$E_s^{dif}(\%) = \frac{\|E_s^{hot} - E_s^{ref}\|_2}{\|E_s^{ref}\|_2} \times 100 \tag{25}$$

Here, E_s^{ref} and E_s^{hot} are scattered field from breast at the normal temperature and the breast after heating process, respectively. A sample heating scenario consisting of realistic breast phantom with tumor and one hotspot region is used for generating E_s^{hot} matrices. Based on this scenario, E_s^{hot} quantities for different dielectric constant-effective conductivity pairs of matching medium are computed by direct scattering solution. Frequency of operation is selected as 1 GHz which is the central frequency for the multi-frequency solutions performed in this paper. Ten values are selected from 5 to 50 with an interval of 5 for dielectric constant, and six values are selected from 0 to 1 with an interval of 0.2 for effective conductivity. For these values of the matching medium, 60 direct scattering solutions are performed at 1 GHz. Next, the difference values are computed with (25), and these values

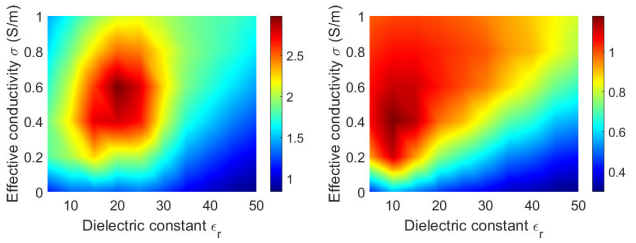

FIGURE 7. Computed difference values by (25) at 1 GHz for each dielectric constant-effective conductivity pair for models with ID number (a) 062204 (b) 012204.

are plotted as 2-D colored images for the distributions used in this paper. Fig. 7 shows said distributions for the selected two breast types.

In Fig. 7, while the blue regions indicate that the dielectric property pair for matching medium giving poor results, the dielectric property pairs corresponding to the red colored regions indicate a better penetration. In [29] and [30], 2.6 value for dielectric constant of matching medium is used. However, when used in this work this value does not give a physically meaningful result. Also, this is consistent with the obtained results in Fig. 7. In addition, a method to determine proper matching medium is presented in [31]. Since a lossless medium is assumed in this work, specified dielectric property values does not provide accurate results. As it can be seen from Fig. 7, non-conductive matching mediums decrease the accuracy and correspond to the blue regions. We should note that this conclusion is also consistent with our experiences.

Based on Fig. 7, we selected matching media as $\epsilon_{r_b} = 20$ and $\sigma_b = 0.6$ for the model 062204, and $\epsilon_{r_b} = 10$ and $\sigma_b = 0.4$ for the model 012204. Note that it can not be said that these values are optimal because proposed algorithm depends on different factors such as regularization parameter and maximum number of iteration. However, it can be inferred that these values are one of the best values among all possible choices.

The proposed approach for matching medium selection in this paper can be considered as costly from computational aspect since direct scattering simulations must be performed for each dielectric constant-conductivity pair. Particularly for 3-D simulations, computational cost will be larger than 2-D case. However, as stated before, changes on dielectric properties due to temperature are limited. Thus, penetration of the EM wave into breast interior is of vital importance to obtain accurate results. This means that matching medium selection deserves a special attention. From another perspective, simulations performed for matching medium selection process are realized before the treatment application; therefore, it has not any effect on computational cost of the imaging algorithm.

III. RESULTS

A. 2-D BREAST PHANTOM

The iterative process in the proposed algorithm has two termination criteria. Firstly, when value of the cost function

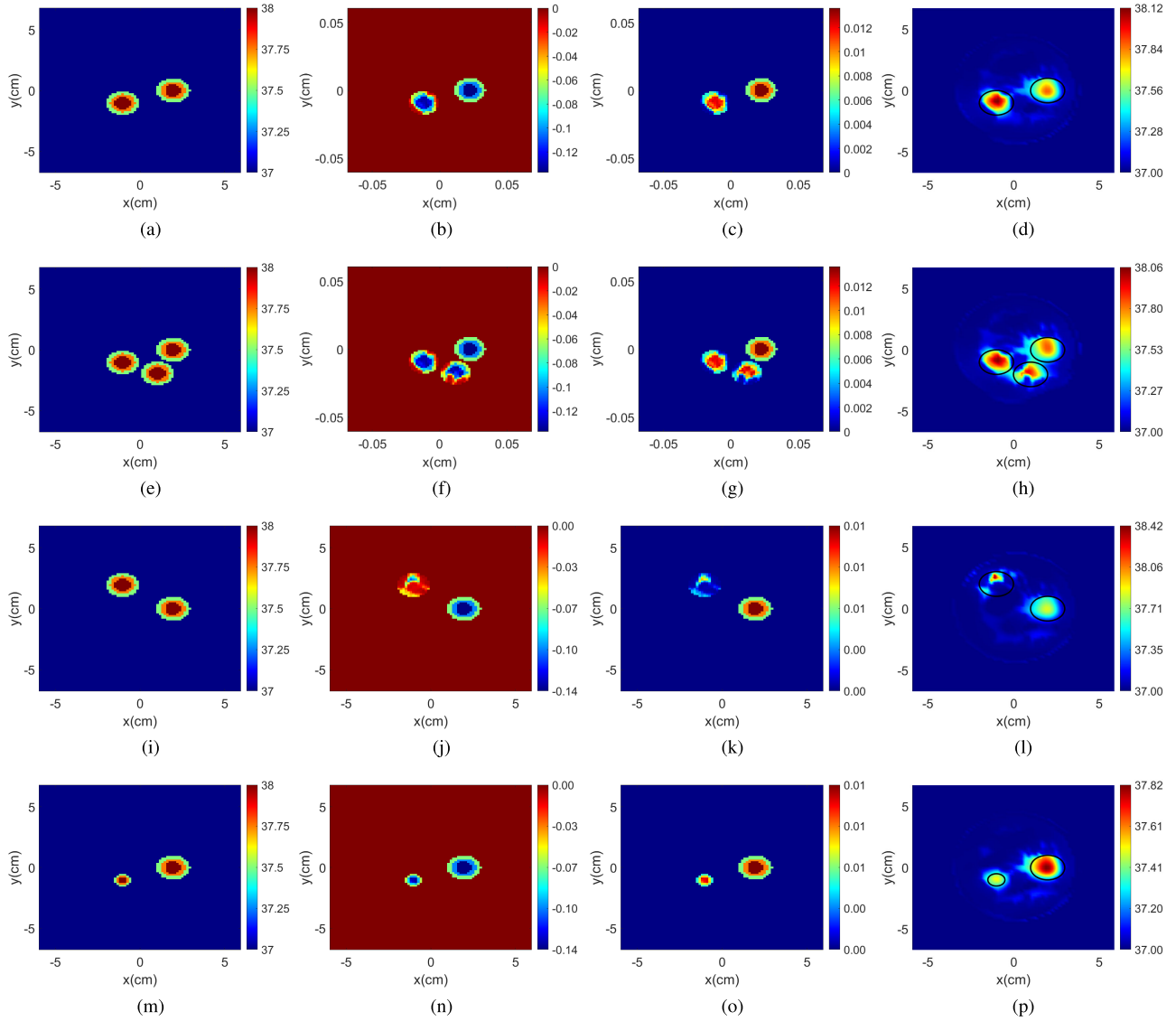

FIGURE 8. Different heating scenarios and reconstruction results on model with ID: 062204 for noise free case. (a),(e),(i),(m) Temperature map on the breast for different heating scenarios in which top temperature is 38°C. Corresponding changes on (b),(f),(j),(n) dielectric constant and (c),(g),(k),(o) effective conductivity due to the temperature variation from 37°C to 38°C. (d),(h),(l),(p) Reconstruction results (°C) obtained by the algorithm. Note that the black circles enclose the regions in where temperature was changed.

starts to increase, the algorithm stops the iteration, and the temperature estimation in the previous step is accepted as final estimation of the algorithm. Second criteria is the maximum number of iterations, which is denoted by N_{max} and fixed to 20 for all the scenarios presented in this paper. However, the algorithm converges in a few iteration steps for almost all investigated scenarios thanks to the optimum parameter selection performed via the L-curve method.

As a figure of merit for the imaging results, a well-known error function given below with (26) is used.

$$e_T(\%) = \frac{\|\boldsymbol{T}_{exact} - \boldsymbol{T}_t\|_2}{\|\boldsymbol{T}_{exact}\|_2} \times 100 \tag{26}$$

Here, $\boldsymbol{T}_{exact}, \boldsymbol{T}_t \in \mathbb{R}^N$ denote exact and reconstructed temperature distributions, respectively. In addition, it is also important to give another figure of merit based on the maximum values of estimated temperature on the heated regions. Because maximum values of estimated temperature are indicators of danger on healthy tissue or proper heating on the tumor. Therefore, we define another error function indicating the relative difference between exact and reconstructed temperature maxima on all heated regions as follows:

$$e_{T_{max}}(\%) = \frac{\|\boldsymbol{T}_{exact_{max}} - \boldsymbol{T}_{t_{max}}\|_2}{\|\boldsymbol{T}_{exact_{max}}\|_2} \times 100 \tag{27}$$

in which $\boldsymbol{T}_{exact_{max}}, \boldsymbol{T}_{t_{max}} \in \mathbb{R}^k$ are the vectors of exact and estimated maximum temperatures, where k denotes the total number of heated regions (the tumor and hotspot/s).

TABLE 1. Reconstruction errors for noise-free cases given in Fig. 8.

Case	$e_T(\%)$	$e_{T_{max}}(\%)$
1. Fig 8(a)-(d)	0.1562	0.3205
2. Fig 8(e)-(h)	0.2243	0.2829
3. Fig 8(i)-(l)	0.2462	0.8317
4. Fig 8(m)-(p)	0.1456	0.9714

First results are obtained for the heterogeneously dense model with Breast ID: 062204 in noise-free case. A circular tumor with a radius of 1 cm is added to the location $(x, y) = (2, 0)$ cm. Reconstruction results for different heating scenarios are given in Fig. 8. In the first case given in Fig. 8(a)-(d), there is one hotspot region with a radius of $r_h = 1$ cm located at $(x, y) = (-1, -1)$ cm. In second case which is given in Fig. 8(e)-(h), there are two hotspots on glandular dense tissue regions located at $(x, y) = (-1, -1)$ cm and $(x, y) = (1, -2)$ cm where radii of both regions are $r_h = 1$ cm. In the third case given in Fig. 8(i)-(l), a hotspot with same size is replaced on a highly fatty region located at $(x, y) = (-1, 2)$ cm. Finally, in the fourth case given in Fig. 8(m)-(p), there is also one hotspot but its radius is reduced to $r_h = 0.5$ cm, and it is located at $(x, y) = (-1, -1)$ cm. Based on the given results, it can be inferred that temperature is poorly estimated for heated regions emerged on fatty tissues because temperature variation model used in this paper is based on percentage. That means changes due to temperature on dielectric property of tissue regions with low dielectric profile such as fat tissues may be very low. This can be especially seen from the figures in second and third columns in Fig. 8. As a result, the algorithm does not 'see' effect of these regions since their contribution on the scattered field data are very low. It is reasonable to think that the inversion method filters this small changes. Especially, there are greater fatty regions for the second and third cases; therefore, calculated reconstruction errors ($e_T(\%)$) for these cases are higher than others as it is seen from Table 1.

As second example, noisy cases are also investigated. Firstly, in a practical scenario, the digital phantom derived via MRI should have an error. Thus, we add uniform error to the reference electrical property distribution:

$$\widetilde{\boldsymbol{\xi}}_f = (1 + \boldsymbol{r}_{v_f})\boldsymbol{\xi}_f. \tag{28}$$

Here, $\boldsymbol{r}_{v_f} \in \mathbb{R}^N$ is error coefficient vector in percentage in which upper bound is denoted by a_e, and it is given by

$$\boldsymbol{r}_{v_f} = \frac{-a_e + 2a_e\boldsymbol{r}_a}{100} \tag{29}$$

where $\boldsymbol{r}_a \in \mathbb{R}^N$ is a vector containing random numbers between 0 and 1. Secondly, measured scattered fields from normal and heated breast are also assumed to be noisy. These noises are taken as white Gaussian noise (AWGN), and same dB value is used for both the scattered field matrices.

First examination with noise is based on the heating scenario given in Fig. 8(a)-(d). Reconstructions at 38°C for different SNR-a_e pairs are performed, and error functions given with (26) and (27) are calculated. In order to obtain more reliable results, this process is repeated 10 times, and mean value of these 10 results is used as final result. The reconstruction errors are given in Fig. 9. Firstly, a safety zone can be determined from these error distributions. We have observed that good estimations are generally obtained for $e_T < 0.3\%$ and $e_{T_{max}} < 0.5\%$. Then, 35-40 dB SNR value can be considered as a lower bound for a good reconstruction result for 1°C resolution with the model ID: 062204. Therefore, we can define the safety zone as SNR $\geq$ 40 dB. Secondly, in the safety zone, both errors are almost independent from the uniform error on the reference distribution (a_e). (It should be noted that we do not focus on the region under the safety zone because these high error values are originated from divergent solutions, which do not give any physically meaningful estimation.) The main reason for this situation is that the algorithm does not use any computed scattered field from solution of the noisy dielectric property distribution from MRI ($\widetilde{\boldsymbol{\xi}}_f$). (The breast is assumed to be measured at both normal and hot states. Thus, there is no need to evaluate the scattered field for normal state.) Dielectric property distribution from MRI ($\widetilde{\boldsymbol{\xi}}_f$) is only used in computation of the reference total field, which can be denoted by $\widetilde{E}_f^{ref}$ in noisy case.

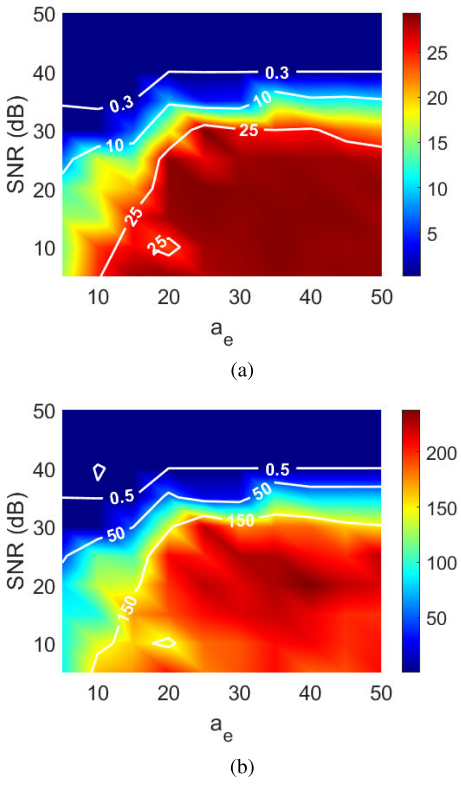

FIGURE 9. Reconstruction errors calculated by (a) (26) and (b) (27) for different a_e and SNR values.

Reconstruction results at different temperatures and different SNR values are also given in Fig. 10(a)-(d) for

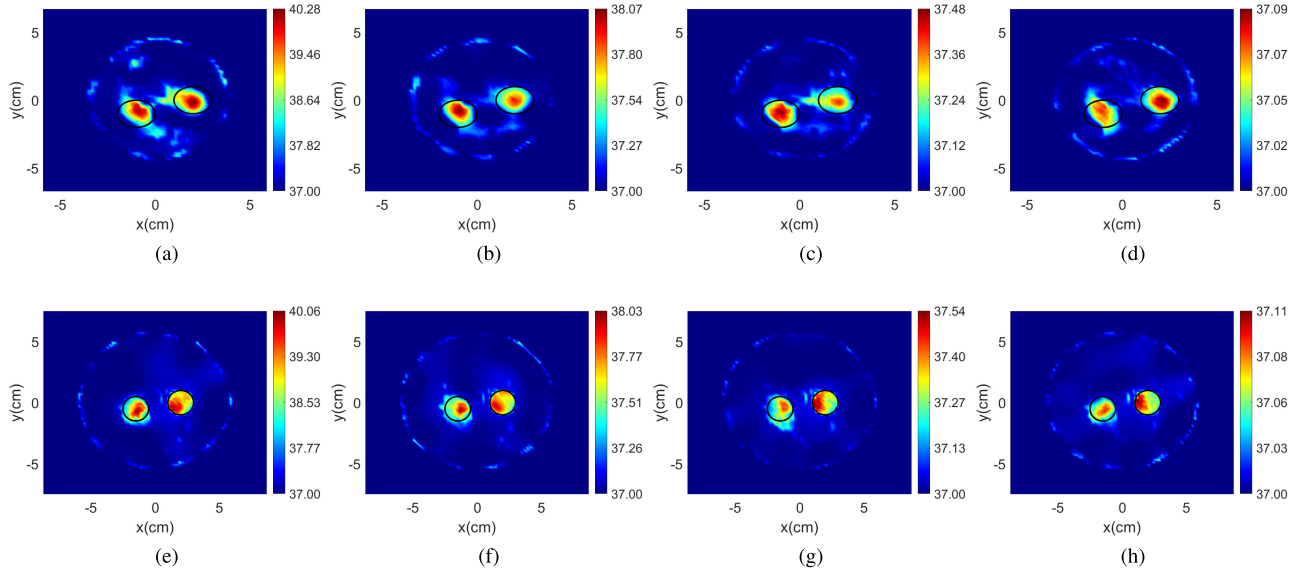

FIGURE 10. Reconstructions (°C) in noisy case at 40°C, 38°C, 37.5°C, and 37.1°C (from left to right), respectively. (a)-(d) The model with ID: 062204 for (a) 30 dB, (b) 40 dB, (c) 50 dB, and (d) 60 dB white Gaussian noise. (e)-(h) The model with ID: 012204 for (e) 40 dB, (f) 50 dB, (g) 60 dB, and (h) 70 dB white Gaussian noise.

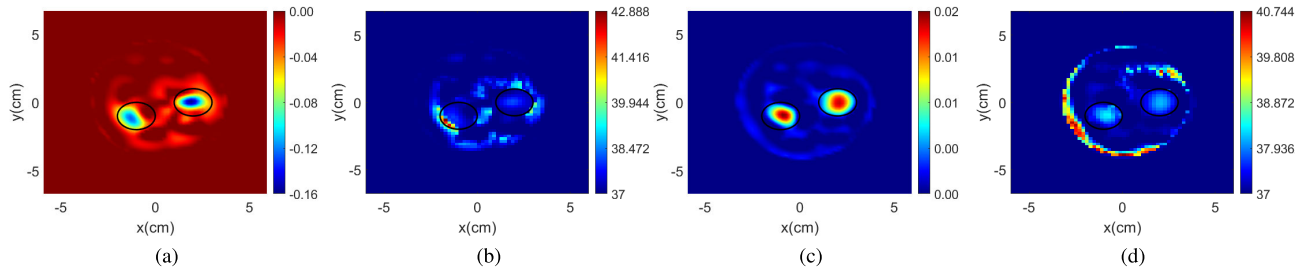

FIGURE 11. Noise-free reconstructions obtained by DBIM for the heating scenario given in Fig. 8(a)-(d). (a) The reconstructed dielectric constant ($\delta\epsilon_r$) and (b) the estimated temperature distribution (°C) mapped from (a). (c) The reconstructed effective conductivity ($\delta\sigma$) and (d) the estimated temperature distribution (°C) mapped from (c).

062204 model, and in Fig. 10(e)-(h) for 012204 model. We selected four different temperature values as 40°C, 38°C, 37.5°C, and 37.1°C; thus, these values indicate the resolutions 3°C, 1°C, 0.5°C, and 0.1°C since reference distribution is assumed at 37°C. In here, we search minimum SNR value for good reconstructions at each resolution. (E.g., Fig. 10-(a), for 3°C temperature difference, good reconstructions can be obtained with minimum SNR of 30 dB; thus, the result for 30 dB is given.) The upper bound of distribution error is fixed at $a_e = 10$, which means noisy values of each cell can change between -10% and +10% of noiseless distribution. From the Fig. 10, it can be seen that tumor and hotspot regions are distinguishable, and the results are comparable with noise-free case. In addition, the 012204 model is more sensitive to noise. This is probably originated from differences in size of the cross sections and glandular/fat ratio between the models.

We mentioned that rearranging the equations to directly obtain the temperature difference improves the results. To see this, the transition from dielectric property estimation to temperature estimation, which is a general approach in the literature, is also considered. The DBIM is utilized for the estimation of the real and imaginary parts of the contrast difference vector ($\delta\boldsymbol{\xi}$), and the obtained solutions are mapped to temperature by the temperature variation model assumed during the study. The results are given in the Fig. 11. It is worth noting that the inversion is performed to obtain the real and imaginary parts of the $\delta\boldsymbol{\xi}$. We have treated the imaginary part as unknown instead of effective conductivity because small values of effective conductivity can cause large numerical errors. (However, the distribution given in Fig. 11(c) belongs to effective conductivity.) Firstly, it can be said that the dielectric properties, especially the effective conductivity, are estimated with reasonably good accuracy. On the other hand, the accuracy of the results for temperature distributions is very low, and this is mainly due to the overestimated temperatures, especially on the fatty tissues. Since our temperature model is based on a relative percentage

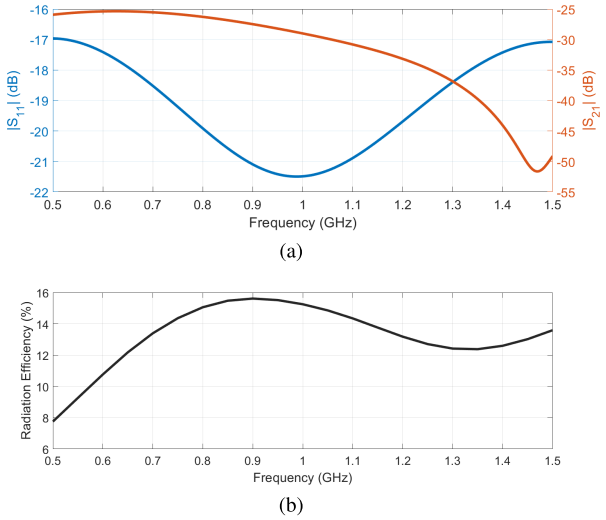

FIGURE 12. Variation of some parameters of the dipole antenna used in the simulations. (a) S_{11} and S_{21}. (b) Radiation efficiency.

change, even if the dielectric property change values are small, these values can be mapped to large values in terms of temperature due to the low dielectric properties of the fatty tissues. Therefore, there are many overestimated temperature values in Fig. 11(b) and Fig. 11(d). The reconstruction errors are $e_T = 1.0171\%$ and $e_{T_{max}} = 9.1012\%$ for Fig. 11(b) and $e_T = 1.1635\%$ and $e_{T_{max}} = 0.7571\%$ for Fig. 11(d). If these values are compared with the first row of Table 1, it can be said that the proposed approach is superior to the common approach in the literature, in which temperature estimation is carried out by external mapping of dielectric properties to temperature. Another disadvantage of the external mapping is ambiguity about which temperature distribution will be accepted, i.e., Fig. 11(b) or Fig. 11(d). The given results show that the temperature distribution mapped from effective conductivity is more accurate, especially when only heated regions are considered; however, it is questionable whether this can be generalized.

We did not perform detailed exploration for speed of the algorithm. However, as it is stated before, the BIM-based algorithm does not need to solve direct scattering problem during the inversion process, which is main advantage of the algorithm in terms of computation time. To obtain the results given in the paper, a laptop with Intel Core i7-11800H @ 2.30 GHz processor has been used. The algorithm converges to minimum error in a few iteration step. Mean values of the computation time for temperature estimation have been approximately calculated as 0.191 s and 0.273 s for the models with ID: 062204 and ID: 012204, respectively. These values show that the proposed method can be considered as a candidate for real-time monitoring applications.

B. 3-D BREAST PHANTOM

The proposed algorithm is also applied to the scattered field data calibrated from S-parameters computed via CST

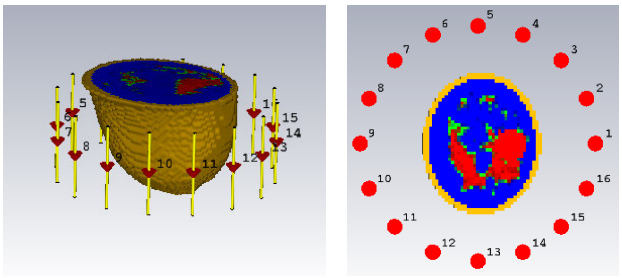

FIGURE 13. The breast model imported to the CST program. (a) Front view and the antennas. (b) Top view of the cross-section at $z = 20$ mm.

Studio software. For this purpose, the breast model with ID: 062204, is imported as a voxel data to the CST. Number of different material can not be greater than 255 in the CST program; therefore, a rounding process is applied to the actual breast model to reduce the number of materials. This is simply rounding the real and imaginary parts of complex relative permittivity value of each cell to nearest integer value. Matching media is selected with the same value in 2-D case, i.e., $\epsilon_r = 20$ and $\sigma = 0.6$. The antennas used in the simulations are identical dipole antennas having resonance frequency around 1 GHz. As an example, S_{11} and S_{21} variations are given in Fig. 12(a). From this variations, it can not be said that the antennas have a perfect matching at these frequencies. Radiation efficiency plot given in Fig. 12(b) shows that the very low S_{11} values are originated from the high losses due to highly conductive matching medium. Therefore, a significant part of the power is converted into heat, and the radiation efficiency is only around 13%. This is main disadvantage of high loss matching mediums from practical aspect. The analysis frequencies are same with 2-D case, i.e., from 500 MHz to 1500 MHz with 100 MHz step size. Length, radius and the gap in excitation port are 57.65 mm, 1 mm, and 3.352 mm for the antennas, respectively. The centers of the antennas are on plane of $z = 20$ mm, which is also the cross-section used for 2-D analysis performed for the model 062204 in Section III-A. The imported model and the antennas can be seen in Fig. 13.

Four different S-parameter data are calculated via time domain simulations in the CST and exported as touchstone files. First one is when there is no scatterer in the investigation region, and it is denoted as S_{empty}. Another one is from a long perfectly conducting circular cylinder with a radius of 5 cm, which is denoted by S_{metal}. Third and fourth one is denoted by S_{ref} and S_{hot} indicating S-parameter data obtained at normal temperature and the temperature after the heating process, respectively. Then, scattered S-parameters for each measurement are calculated as follows:

$$S_{metal}^{scatt} = S_{metal} - S_{empty} \tag{30}$$
$$S_{ref}^{scatt} = S_{ref} - S_{empty} \tag{31}$$
$$S_{hot}^{scatt} = S_{hot} - S_{empty} \tag{32}$$

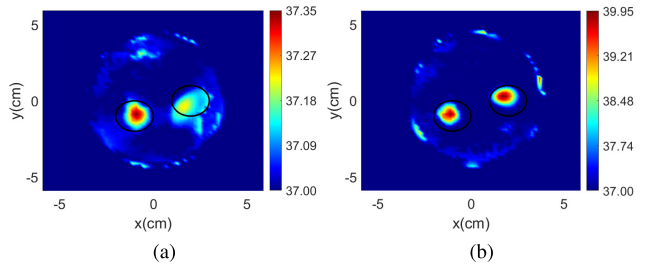

FIGURE 14. Reconstruction results (°C) obtained from the calibrated scattered field data from CST program. (a) Maximum temperature is 38°C and SNR is 85 dB. (b) Maximum temperature is 45°C and SNR is 65 dB.

Then, calibrated differential scattered electric field between heated and normal breasts can be calculated as,

$$E_{dif}^{scatt} = \frac{S_{hot}^{scatt} - S_{ref}^{scatt}}{S_{metal}^{scatt}} E_{metal}^{scatt} \tag{33}$$

where E_{metal}^{scatt} indicates the scattered field from 2-D perfectly conducting cylinder with a radius of 5 cm, when it is illuminated with infinitely long current sources positioned on a circle, whose center is at origin and radius is 7.5 cm. Note that all of these quantities are frequency dependent, but frequency index is omitted to simplify the notation. At the end of this operation, E_{dif}^{scatt} has dimension of $16 \times 16 \times 11$, similar to the scattered electric fields used in 2-D case examples.

We consider the same case given in Fig. 8(a) where there is one tumor, and one hotspot in the breast interior. (The only difference from Fig. 8(a) is that the tumor and hotspot is a sphere with a radius of 1 cm, not a cylinder.) Two different heating cases are considered in which maximum temperature value inside the breast are 38°C and 45°C. Simulations are performed for each case, and the calibrated scattered matrices are processed by the proposed algorithm. The SNR values are 85 dB and 65 dB for 38°C and 45°C cases, respectively. (Note that we do not add any noise on reference distribution for CST simulations because there are already round-off errors on the distribution due to the limited number of imported material to the program.) The obtained results are given in Fig. 14. The results show that locations of the heated regions are accurately estimated. However, the estimated temperature values highly differ from the exact temperature values. This is possibly due to differences between 2-D and 3-D field computations. 2-D inversion 'averages' the 3-D contrast difference in z-direction. Thus, it is normal to have underestimated temperature value. Also, we see that the good results are obtained for higher SNR values than 2-D case. This is also originated from the same reason, which is discrepancy between 3-D data and 2-D inversion algorithm. On the other hand, the ratio of the estimated and the exact temperature differences for Fig. 14(a) and Fig. 14(b) are $0.35/1 = 0.35$ and $2.95/8 \approx 0.368$, respectively. These results are very close each other; therefore, it can be considered that there may be an approximate linear relation between the estimated and real temperature differences.

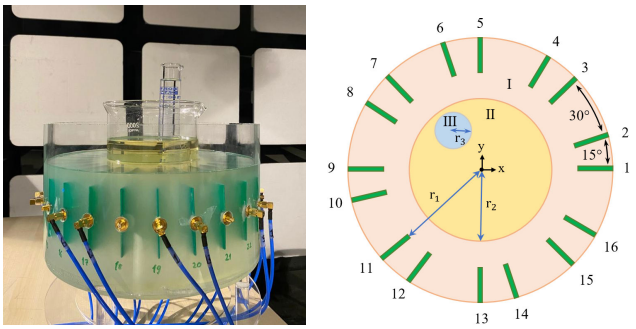

FIGURE 15. (a) A photograph and (b) drawing of the top view of the measurement setup. The antennas are shown with green rectangles and buried in region I, which is filled with triton. The large beaker encloses the region II, which is used to mimic breast phantom and filled with sunflower oil. The thin beaker, which represents the heated tumor, encloses the region III, which is filled with NaCl solution. The heating scenario is handled by changing the concentration of NaCl. Distances are $r_1 = 11$ cm, $r_2 = 6$ cm, and $r_3 = 0.79$ cm.

C. EXPERIMENT RESULTS

Feasibility of the algorithm is also shown by experiments performed with a measurement setup given in Fig. 15(a). The measurement setup consists of beakers, which are placed inside a container. The container is filled with triton, which is used as a matching medium. A large beaker with a radius of 6 cm is used to mimic the breast phantom, and it is filled with sunflower oil. Also, a thin beaker with a radius of 0.79 cm is used to mimic the breast tumor, and this beaker is filled with NaCl solution. In the measurement setup, there are 24 antennas in total; however, we use 16 of them for this work. The ports of the antennas are on a circle with a radius of 11 cm, which is radius of the container. The antennas are identical antipodal Vivaldi antennas. Top view of the setup is given in Fig. 15(b).

Dielectric properties of sunflower oil and triton are measured by a commercially available 3.5 mm dielectric assessment kit from the speag [56] and a network analyzer (Keysight FieldFox). These variations with respect to frequency can be seen in Fig.16(a)-(d). Dielectric properties of NaCl solutions with different concentrations are adopted from [55], and given in Fig. 16(e)-(f). Like the given temperature variations in Section II-A3, dielectric constant decreases and effective conductivity increases with increase on concentration of the solution. Therefore, NaCl solutions with different concentrations are used to model temperature variation on the tumor. The thin beaker is filled with 0.1 mol/L solution to imitate the normal (reference) case, and filled with 0.2 mol/L solution to imitate the heated case. On the other hand, the coefficient vectors, which are previously denoted as $\boldsymbol{\kappa}_f^{\epsilon_r}$ and $\boldsymbol{\kappa}_f^{\sigma}$, must be determined for this model. We calculated the changes on dielectric constant and effective conductivity at 1 GHz as $((76.0425-77.4721)/76.0425)\times 100 = -1.88\%$ and $((2.14135 - 1.19837)/1.19837) \times 100 = +78.6886\%$, respectively. We assume that this variations indicate the 8°C change; therefore, percentage changes per 1°C are calculated as -0.235% and $+9.836\%$. Then, the coefficient vectors for

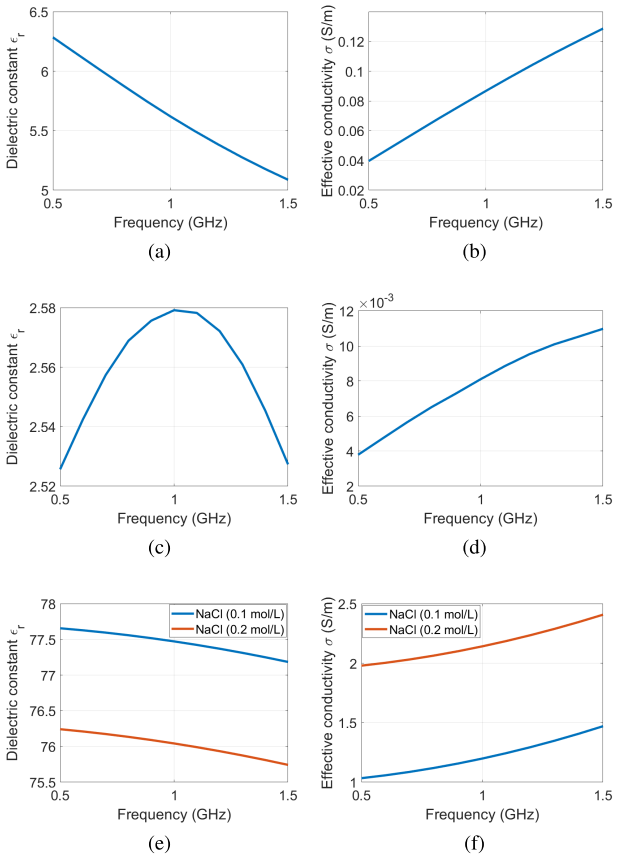

FIGURE 16. Dielectric property variations between 0.5-1.5 GHz. (a) Dielectric constant of triton (measured). (b) Effective conductivity of triton (measured). (c) Dielectric constant of sunflower oil (measured). (d) Effective conductivity of sunflower oil (measured). (e) Dielectric constant of NaCl [55]. (f) Effective conductivity of NaCl [55].

this model are approximately given as

$$\kappa_{exp}^{\epsilon_r} = -0.235 \times 10^{-2} \boldsymbol{\epsilon}_r^{exp} \tag{34}$$

$$\kappa_{exp}^{\sigma} = 9.836 \times 10^{-2} \boldsymbol{\sigma}^{exp} \tag{35}$$

where the frequency indices are omitted for simplicity of the notation. In addition, $\boldsymbol{\epsilon}_r^{exp}$ and $\boldsymbol{\sigma}^{exp}$ denote dielectric property distributions at normal (reference) case for the experimental setup.

Multi-static measurements are collected by the Keysight M9370A PXI Vector Network Analyzers [57] with input power of 10 dBm, and the calibrated scattered field data are obtained via the same approach given in Section III-B. The measurements are carried out for two different scenario, in which the thin beaker is either located at $(x, y) = (3, 1)$ cm or $(x, y) = (-1.5, 2.5)$ cm. The results can be seen in Fig. 17, and they show that location and the radius of the heated regions are determined well. On the other hand, the estimated temperature values are quite far from the true value, which is 45°C. However, this is probably due to the same reason stated in Section III-B. In a 2-D problem, the scatterers are assumed to be infinitely long cylinders, but they have finite length in practice even though they have a

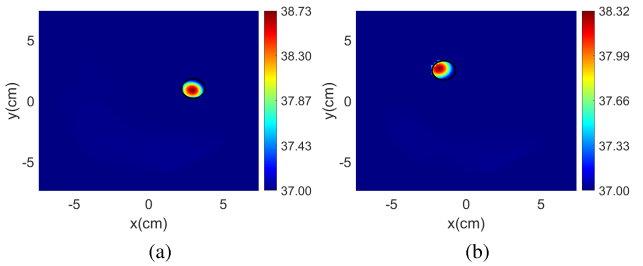

FIGURE 17. Reconstruction results (°C) for the experimental data in which the temperature on the tumor (the thin beaker), which is enclosed by the black circle, is 45°C. The tumor is located at (a) $(x, y) = (3, 1)$ cm, and (b) $(x, y) = (-1.5, 2.5)$ cm.

cylindrical structure. These results can also be compared with the result given in Fig. 14(b), and it can be deduced that the underestimation of the temperature value is originated from the similar reasons in addition to modelling errors.

IV. CONCLUSION

In this paper, a study is presented for quantitative estimation of temperature distribution during breast hyperthermia treatments. Firstly, a model defining the relation between temperature and dielectric properties for breast tissues is given. Based on this model, a BIM-based approach, in which temperature changes are obtained directly, is presented. In addition, an approach to determine proper matching medium in hyperthermia monitoring applications is also given. Feasibility of the algorithm is also shown via calibrated data from CST program and a simple measurement setup, which mimics a breast structure.

The results show that the method provide quantitative information about temperature distribution, which is our main focus in this paper. The computation times during the inversion method show that the algorithm is a candidate for real-time imaging. The analysis about matching medium indicates that a highly conductive matching medium may be necessary to extract information from interior of a realistic breast structure. However, a conductive matching medium will decrease the received signal level; therefore, the system may be very sensitive to noise, which is main issue in a practical implementation.

Our future work will focus on more realistic scenarios, where reconstructions are directly carried out with 3-D scattered field data.

REFERENCES

[1] H. P. Kok, E. N. K. Cressman, W. Ceelen, C. L. Brace, R. Ivkov, H. Grull, G. Ter Haar, P. Wust, and J. Crezee, "Heating technology for malignant tumors: A review," *Int. J. Hyperthermia*, vol. 37, no. 1, pp. 711–741, Jan. 2020, doi: 10.1080/02656736.2020.1779357.

[2] M. Haynes, J. Stang, and M. Moghaddam, "Real-time microwave imaging of differential temperature for thermal therapy monitoring," *IEEE Trans. Biomed. Eng.*, vol. 61, no. 6, pp. 1787–1797, Jun. 2014.

[3] C. J. Simon, D. E. Dupuy, and W. W. Mayo-Smith, "Microwave ablation: Principles and applications," *RadioGraphics*, vol. 25, pp. 69–83, Oct. 2005, doi: 10.1148/rg.25si055501.

[4] G. C. Van Rhoon, M. M. Paulides, T. Drizdal, and M. Franckena, "Hyperthermia and the need to monitor temperature," in *Proc. Int. Conf. Electromagn. Adv. Appl. (ICEAA)*, Sep. 2015, pp. 1181–1185.

[5] C. L. Brace, "Temperature-dependent dielectric properties of liver tissue measured during thermal ablation: Toward an improved numerical model," in *Proc. 30th Annu. Int. Conf. IEEE Eng. Med. Biol. Soc.*, Aug. 2008, pp. 230–233.

[6] C. Rossmann and D. Haemmerich, "Review of temperature dependence of thermal properties, dielectric properties, and perfusion of biological tissues at hyperthermic and ablation temperatures," *Crit. Rev. Biomed. Eng.*, vol. 42, pp. 467–492, Jun. 2014.

[7] N. R. Datta, S. G. Ordóñez, U. S. Gaipl, M. M. Paulides, H. Crezee, J. Gellermann, D. Marder, E. Puric, and S. Bodis, "Local hyperthermia combined with radiotherapy and-/or chemotherapy: Recent advances and promises for the future," *Cancer Treatment Rev.*, vol. 41, no. 9, pp. 742–753, Nov. 2015, doi: 10.1016/j.ctrv.2015.05.009.

[8] P. T. Nguyen, A. Abbosh, and S. Crozier, "Microwave hyperthermia for breast cancer treatment using electromagnetic and thermal focusing tested on realistic breast models and antenna arrays," *IEEE Trans. Antennas Prop.*, vol. 63, no. 10, pp. 4426–4434, Oct. 2015.

[9] Z. Vujaskovic and C. W. Song, "Physiological mechanisms underlying heat-induced radiosensitization," *Int. J. Hyperthermia*, vol. 20, no. 2, pp. 163–174, Mar. 2004, doi: 10.1080/02656730310001619514.

[10] F. Ferraioli, A. Formisano, and R. Martone, "Effective exploitation of prior information in electrical impedance tomography for thermal monitoring of hyperthermia treatments," *IEEE Trans. Magn.*, vol. 45, no. 3, pp. 1554–1557, Mar. 2009.

[11] M. W. Dewhirst, B. L. Viglianti, M. Lora-Michiels, M. Hanson, and P. J. Hoopes, "Basic principles of thermal dosimetry and thermal thresholds for tissue damage from hyperthermia," *Int. J. Hyperthermia*, vol. 19, no. 3, pp. 267–294, Jan. 2003, doi: 10.1080/0265673031000119006.

[12] J. C. Bolomey, L. Jofre, and G. Peronnet, "On the possible use of microwave-active imaging for remote thermal sensing," *IEEE Trans. Microw. Theory Techn.*, vol. MTT-31, no. 9, pp. 777–781, Sep. 1983.

[13] J. Jiang, C. Brace, A. Andreano, R. DeWall, N. Rubert, T. Fisher, T. Varghese, F. Lee, and T. J. Hall, "Elastic modulus imaging (EMI) for visualizing thermal ablation zone: Initial experience in a porcine model," in *Proc. IEEE Int. Ultrason. Symp.*, Mar. 2009, pp. 143–146.

[14] D. Liu and E. S. Ebbini, "Real-time 2-D temperature imaging using ultrasound," *IEEE Trans. Biomed. Eng.*, vol. 57, no. 1, pp. 12–16, Jan. 2010.

[15] L. Xu and X. Wang, "Focused microwave breast hyperthermia monitored by thermoacoustic imaging: A computational feasibility study applying realistic breast phantoms," *IEEE J. Electromagn., RF Microw. Med. Biol.*, vol. 4, no. 2, pp. 81–88, Jun. 2020.

[16] D. Arora, D. Cooley, T. Perry, J. Guo, A. Richardson, J. Moellmer, R. Hadley, D. Parker, M. Skliar, and R. B. Roemer, "MR thermometry-based feedback control of efficacy and safety in minimum-time thermal therapies: Phantom and in-vivo evaluations," *Int. J. Hyperthermia*, vol. 22, no. 1, pp. 29–42, Jan. 2006, doi: 10.1080/02656730500412411.

[17] Z. Li, M. Vogel, P. F. Maccarini, V. Stakhursky, B. J. Soher, O. I. Craciunescu, S. Das, O. A. Arabe, W. T. Joines, and P. R. Stauffer, "Improved hyperthermia treatment control using SAR/temperature simulation and PRFS magnetic resonance thermal imaging," *Int. J. Hyperthermia*, vol. 27, no. 1, pp. 86–99, Feb. 2011, doi: 10.3109/02656736.2010.501509.

[18] R. M. Davis, B. L. Viglianti, P. Yarmolenko, J.-Y. Park, P. Stauffer, D. Needham, and M. W. Dewhirst, "A method to convert MRI images of temperature change into images of absolute temperature in solid tumours," *Int. J. Hyperthermia*, vol. 29, no. 6, pp. 569–581, Sep. 2013, doi: 10.3109/02656736.2013.790091.

[19] K.-J. Lee, J.-Y. Kim, B.-R. Kim, S.-I. Jeon, N. Kim, and S.-H. Son, "Real-time 2D microwave differential imaging for temperature monitoring," in *Proc. Int. Symp. Antennas Propag. (ISAP)*, 2018, pp. 1–2.

[20] T. F. A. Zanoon, "Microwave tomography of thermal breast ablation featuring quantitative image reconstruction: A numerical study," in *Proc. IEEE Int. Conf. Smart Instrum., Meas. Appl. (ICSIMA)*, Aug. 2019, pp. 1–6.

[21] G. Chen, J. Stang, M. Haynes, E. Leuthardt, and M. Moghaddam, "Real-time three-dimensional microwave monitoring of interstitial thermal therapy," *IEEE Trans. Biomed. Eng.*, vol. 65, no. 3, pp. 528–538, Mar. 2018.

[22] R. Scapaticci, G. G. Bellizzi, M. Cavagnaro, V. Lopresto, and L. Crocco, "Exploiting microwave imaging methods for real-time monitoring of thermal ablation," *Int. J. Antennas Propag.*, vol. 2017, pp. 1–13, Nov. 2017, doi: 10.1155/2017/5231065.

[23] P. M. Meaney, M. W. Fanning, K. D. Paulsen, D. Li, S. A. Pendergrass, Q. Fang, and K. L. Moodie, "Microwave thermal imaging: Initialin vivo experience with a single heating zone," *Int. J. Hyperthermia*, vol. 19, no. 6, pp. 617–641, Nov. 2003, doi: 10.1080/0265673031000140822.

[24] R. Scapaticci, V. Lopresto, R. Pinto, M. Cavagnaro, and L. Crocco, "Monitoring thermal ablation via microwave tomography: An ex vivo experimental assessment," *Diagnostics*, vol. 8, no. 4, p. 81, Dec. 2018. [Online]. Available: https://www.mdpi.com/2075-4418/8/4/81

[25] P. M. Meaney, K. D. Paulsen, M. W. Fanning, D. Li, and Q. Fang, "Image accuracy improvements in microwave tomographic thermometry: Phantom experience," *Int. J. Hyperthermia*, vol. 19, no. 5, pp. 534–550, Jan. 2003, doi: 10.1080/0265673031000082386.

[26] G. Bellizzi, O. M. Bucci, and I. Catapano, "Microwave cancer imaging exploiting magnetic nanoparticles as contrast agent," *IEEE Trans. Bio-Med. Eng.*, vol. 58, no. 9, pp. 2528–2536, Sep. 2011.

[27] J. D. Shea, P. Kosmas, B. D. Van Veen, and S. C. Hagness, "Contrast-enhanced microwave imaging of breast tumors: A computational study using 3D realistic numerical phantoms," *Inverse Problems*, vol. 26, no. 7, Jul. 2010, Art. no. 074009. [Online]. Available: https://europepmc.org/articles/pmc2951614?pdf=render, and https://app.dimensions.ai/details/publication/pub.1021285008

[28] F. Gao, B. D. Van Veen, and S. C. Hagness, "Contrast-enhanced microwave imaging of breast tumors using sparsity regularization," in *Proc. IEEE Int. Symp. Antennas Propag.*, Jul. 2012, pp. 1–2.

[29] J. D. Shea, B. D. Van Veen, and S. C. Hagness, "A TSVD analysis of microwave inverse scattering for breast imaging," *IEEE Trans. Biomed. Eng.*, vol. 59, no. 4, pp. 936–945, Apr. 2012.

[30] M. Ambrosanio, P. Kosmas, and V. Pascazio, "A multithreshold iterative DBIM-based algorithm for the imaging of heterogeneous breast tissues," *IEEE Trans. Biomed. Eng.*, vol. 66, no. 2, pp. 509–520, Feb. 2019.

[31] I. Catapano, L. D. Donato, L. Crocco, O. M. Bucci, A. F. Morabito, T. Isernia, and R. Massa, "On quantitative microwave tomography of female breast," *Progr. Electromagn. Res.*, vol. 97, pp. 75–93, Jan. 2009.

[32] Phantom Repository. *University of Wisconsin Cross-Disciplinary Electromagnetics Laboratory*. Accessed: Dec. 30, 2021. [Online]. Available: https://uwcem.ece.wisc.edu/phantomRepository.html

[33] M. Lazebnik, D. Popovic, L. McCartney, C. B. Watkins, M. J. Lindstrom, J. Harter, S. Sewall, T. Ogilvie, A. Magliocco, T. M. Breslin, W. Temple, D. Mew, J. H. Booske, M. Okoniewski, and S. C. Hagness, "A large-scale study of the ultrawideband microwave dielectric properties of normal, benign and malignant breast tissues obtained from cancer surgeries," *Phys. Med. Biol.*, vol. 52, no. 20, pp. 115–6093, 2007. [Online]. Available: https://app.dimensions.ai/details/publication/pub.1059026818

[34] J. S. Michaelson, S. Satija, D. Kopans, R. Moore, M. Silverstein, A. Comegno, K. Hughes, A. Taghian, S. Powell, and B. Smith, "Gauging the impact of breast carcinoma screening in terms of tumor size and death rate," *Cancer*, vol. 98, no. 10, pp. 2114–2124, Nov. 2003. [Online]. Available: https://acsjournals.onlinelibrary.wiley.com/doi/abs/10.1002/cncr.11766

[35] A. Martellosio, M. Pasian, M. Bozzi, L. Perregrini, A. Mazzanti, F. Svelto, P. E. Summers, G. Renne, L. Preda, and M. Bellomi, "Dielectric properties characterization from 0.5 to 50 GHz of breast cancer tissues," *IEEE Trans. Microw. Theory Techn.*, vol. 65, no. 3, pp. 998–1011, Mar. 2017.

[36] K. S. Cole and R. H. Cole, "Dispersion and absorption in dielectrics I. Alternating current characteristics," *J. Chem. Phys.*, vol. 9, no. 4, pp. 341–351, Apr. 1941.

[37] S. Ley, S. Schilling, O. Fiser, J. Vrba, J. Sachs, and M. Helbig, "Ultra-wideband temperature dependent dielectric spectroscopy of porcine tissue and blood in the microwave frequency range," *Sensors*, vol. 19, no. 7, p. 1707, Apr. 2019. [Online]. Available: https://www.mdpi.com/1424-8220/19/7/1707

[38] M. Lazebnik, M. C. Converse, J. H. Booske, and S. C. Hagness, "Ultrawideband temperature-dependent dielectric properties of animal liver tissue in the microwave frequency range," *Phys. Med. Biol.*, vol. 51, no. 7, pp. 55–1941, 2006. [Online]. Available: https://app.dimensions.ai/details/publication/pub.1059026490

[39] E. Zastrow, S. C. Hagness, and B. D. Van Veen, "3D computational study of non-invasive patient-specific microwave hyperthermia treatment of breast cancer," *Phys. Med. Biol.*, vol. 55, no. 13, pp. 3611–3629, Jun. 2010, doi: 10.1088/0031-9155/55/13/003.

[40] M. E. Kowalski and J.-M. Jin, "Determination of electromagnetic phased-array driving signals for hyperthermia based on a steady-state temperature criterion," *IEEE Trans. Microw. Theory Techn.*, vol. 48, no. 11, pp. 1864–1873, Nov. 2000.
[41] J. Richmond, "Scattering by a dielectric cylinder of arbitrary cross section shape," *IEEE Trans. Antennas Propag.*, vol. AP-13, no. 3, pp. 334–341, May 1965.
[42] P. M. Van Den Berg and R. E. Kleinman, "A contrast source inversion method," *Inverse Prob.*, vol. 13, no. 6, p. 1607, Dec. 1997. [Online]. Available: https://app.dimensions.ai/details/publication/pub.1053021326
[43] D. Colton and R. Kress, *Inverse Acoustic and Electromagnetic Scattering Theory*, 3rd ed. New York, NY, USA: Springer, 2013.
[44] W. C. Chew, *Waves and Fields in Inhomogenous Media*. Hoboken, NJ, USA: Wiley, 1999.
[45] S. Dogu, M. Akinci, M. Çayören, and I. Akduman, "Truncated singular value decomposition for through-the-wall microwave imaging application," *IET Microw., Antennas Propag.*, vol. 14, no. 4, pp. 260–267, 2019.
[46] O. M. Bucci, L. Crocco, T. Isernia, and V. Pascazio, "Inverse scattering problems with multifrequency data: Reconstruction capabilities and solution strategies," *IEEE Trans. Geosci. Remote Sens.*, vol. 38, no. 4, pp. 1749–1756, Jul. 2000.
[47] D. W. Winters, J. D. Shea, P. Kosmas, B. D. Van Veen, and S. C. Hagness, "Three-dimensional microwave breast imaging: Dispersive dielectric properties estimation using patient-specific basis functions," *IEEE Trans. Med. Imag.*, vol. 28, no. 7, pp. 969–981, Jul. 2009.
[48] A. N. Tikhonov and V. Y. Arsenin, *Solutions of Ill-Posed Problems*. Washington, DC, USA: Winston, 1977.
[49] P. C. Hansen. (2010). *Discrete Inverse Problems, Society for Industrial and Applied Mathematics*. [Online]. Available: https://epubs.siam.org/doi/abs/10.1137/1.9780898718836
[50] C. Gilmore, P. Mojabi, and J. LoVetri, "Comparison of an enhanced distorted born iterative method and the multiplicative-regularized contrast source inversion method," *IEEE Trans. Antennas Propag.*, vol. 57, no. 8, pp. 2341–2351, Aug. 2009.
[51] P. C. Hansen and D. P. O'Leary, "The use of the L-curve in the regularization of discrete ill-posed problems," *SIAM J. Sci. Comput.*, vol. 14, no. 6, pp. 1487–1503, 1993, doi: 10.1137/0914086.
[52] P. C. Hansen, "Regularization tools version 4.0 for MATLAB 7.3," *Numer. Algorithms*, vol. 46, no. 2, pp. 189–194, Oct. 2007, doi: 10.1007/s11075-007-9136-9.
[53] W. C. Chew and Y. M. Wang, "An iterative solution of the two-dimensional electromagnetic inverse scattering problem," *Int. J. Imag. Syst. Technol.*, vol. 1, pp. 100–108, Jan. 1989. [Online]. Available: https://onlinelibrary.wiley.com/doi/abs/10.1002/ima.1850010111
[54] J. D. Shea, P. Kosmas, S. C. Hagness, and B. D. Van Veen, "Three-dimensional microwave imaging of realistic numerical breast phantoms via a multiple-frequency inverse scattering technique," *Med. Phys.*, vol. 37, no. 8, pp. 4210–4226, 2010. [Online]. Available: https://aapm.onlinelibrary.wiley.com/doi/abs/10.1118/1.3443569
[55] A. Peyman, C. Gabriel, and E. H. Grant, "Complex permittivity of sodium chloride solutions at microwave frequencies," *Bioelectromagnetics*, vol. 28, no. 4, pp. 264–274, 2007. [Online]. Available: https://onlinelibrary.wiley.com/doi/abs/10.1002/bem.20271
[56] *Dielectric Assessment Kit 3.5 (200 MHz - 20 GHz)*. Accessed: Aug. 17, 2022. [Online]. Available: https://speag.swiss/products/dak/dak-probes/
[57] *M9370A PXI Vector Network Analyzer, 300 kHz to 4 GHz*. Accessed: Dec. 22, 2022. [Online]. Available: https://www.keysight.com/us/en/product/M9370A/pxie-vector-network-analyzer-300-khz-to-4-ghz.html

HULUSI ONAL was born in Istanbul, Turkey, in 1996. He received the B.S. degree in electronics and communication engineering from Istanbul Technical University (ITU), Istanbul, in 2019, where he is currently pursuing the M.S. degree in telecommunication engineering. He is a Research and Teaching Assistant with the Electronics and Communication Engineering (ECE) Department, ITU. His main research interests include electromagnetic scattering problems, microwave imaging, and antenna design.

TUBA YILMAZ (Member, IEEE) received the B.S. degree from Istanbul Technical University (ITU), Istanbul, Turkey, in 2007, the M.S. degree from Mississippi State University, Mississippi State, MS, USA, in 2009, and the Ph.D. degree in electronic engineering and computer science from Queen Mary University of London, London, U.K., in 2013.

From 2013 to 2014, she was a Postdoctoral Research Fellow with Utah State University (USU). She is currently an Associate Professor and a Marie Sklodowska Curie Research Fellow with the Department of Electronics and Communication Engineering, ITU. Prior to her appointment with ITU, she spent a year with Mitos Medical Technologies, as an Associate Research Fellow. Her research interests include wearable and implantable antennas, RF sensing, dielectric spectroscopy, evolutionary optimization techniques, wireless power transfer, and microwave imaging. She is a member of the Eta Kappa Nu Electrical and Computer Engineering Honor Society. She has received the URSI Young Scientist Award, in 2017.

MEHMET NURI AKINCI was born in Ankara, Turkey, in 1992. He received the B.Sc. (Hons.) and Ph.D. degrees in electronics and communication engineering from Istanbul Technical University (ITU), Istanbul, Turkey, in 2013 and 2017, respectively.

He was a Visiting Scientist with the Institute for the Electromagnetic Sensing of the Environment, National Research Council of Italy, Naples, Italy, in 2015, and Virginia Commonwealth University, Richmond, VA, USA, in 2016. He is currently an Associate Professor with the Electronics and Communication Engineering Department, ITU. His current research interests include inverse scattering problems, microwave measurement systems, and optics.